energies

MDPI

Article

The Design and Processor-In-The-Loop Implementation of a Super-Twisting Control Algorithm Based on a Luenberger Observer for a Seamless Transition between Grid-Connected and Stand-Alone Modes in Microgrids

Ali Aillane [1], Karim Dahech [1], Larbi Chrifi-Alaoui [2,*], Aissa Chouder [3], Tarak Damak [1], Abdelhak Hadjkaddour [4] and Pascal Bussy [2]

[1] Laboratory of Sciences and Techniques of Automatic Control and Computer Engineering (Lab-STA), National School of Engineering of Sfax (ENIS), University of Sfax, Sfax 3038, Tunisia; ali.aillane@enis.tn (A.A.); karim.dahech@isgis.usf.tn (K.D.); tarak.damak@enis.tn (T.D.)
[2] Laboratory of Innovative Technology (LTI, UR 3899), University of Picardie Jules Verne, 80000 Amiens, France; pascal.bussy@u-picardie.fr
[3] Electrical Engineering Laboratory, University Mohamed Boudiaf of M'sila, M'sila 28000, Algeria; aissa.chouder@univ-msila.dz
[4] Laboratory of Electrical Engineering and Automation, University Yahia Fares Medea, Medea 26000, Algeria; hadjkaddour.abdelhak@univ-medea.dz
* Correspondence: larbi.alaoui@u-picardie.fr

Abstract: The abrupt transfer from grid-connected (GC) to stand-alone (SA) operation modes is one of the major issues that may threaten the stability of a distributed generation (DG) system. Furthermore, if the islanding mode happens, it is vital to take into consideration the load voltages or load current waveforms as soon as feasible. This paper develops an advanced control technique based on a super-twisting sliding mode controller (ST-SMC) for a three-phase inverter operating in both the GC and SA modes. This control scheme is proposed to ensure a smooth transition from the GC to SA mode and enhance the load voltage waveforms under the islanding mode. In addition, to minimize the operational costs of the system and the complexity of the studied model, a digital Luenberger observer (DLO) with a proper design is adopted for estimating the inverter-side current. The control scheme of the whole system switches between a current control mode during the GC mode and a voltage control mode during the SA mode. The super-twisting control algorithm is applied to the outer voltage control loop involved in the cascaded voltage/current control scheme in the SA mode. Simulation tests of a three-phase inverter are performed for the purpose of assessing the suggested control performance by using the PowerSim (PSIM) software and comparing it with a classical PI controller. Furthermore, a processor-in-the-loop (PIL) implementation in a DSP board TMS32F28335 while debugging is conducted using code composer studio 6.2.0. The obtained results show efficient control properties, such as a smooth transition among the microgrid (MG) operating modes, as well as effectiveness and robustness during both the GC and SA operation modes.

Keywords: microgrid; grid-connected mode; islanding mode; smooth transition; super-twisting sliding mode controller; digital Luenberger observer; processor-in-the loop (PIL)

Citation: Aillane, A.; Dahech, K.; Chrifi-Alaoui, L.; Chouder, A.; Damak, T.; Hadjkaddour, A.; Bussy, P. The Design and Processor-In-The -Loop Implementation of a Super-Twisting Control Algorithm Based on a Luenberger Observer for a Seamless Transition between Grid-Connected and Stand-Alone Modes in Microgrids. *Energies* **2023**, *16*, 3878. https://doi.org/10.3390/en16093878

Academic Editor: Nicu Bizon

Received: 16 March 2023
Revised: 10 April 2023
Accepted: 28 April 2023
Published: 3 May 2023

1. Introduction

Currently, microgrids (MG) are viewed as an attractive and efficient solution for adapting renewable energy sources inside a large distributed generation (DG) system, which is able to assist the grids by distributing the load and decreasing the grids' requirements [1]. In addition to making the client more reliable and the system extra useful, the DG's capacity to function in both a centralized and decentralized way increases the user's autonomy [2]. Furthermore, MGs have an important advantage, which is their capability to operate in both

GC and SA modes [3]. Renewable resources are adopted into an MG via electrical power converters, most notably inverters. In the GC mode, the inverter-based DGs send active and reactive electricity to the local grid. The DGs are connected to the grid during centralized operation and their voltage and frequency are synchronized with the grid. However, if the DGs are unable to restore the system to grid standards due to a grid failure, the grid is quickly disconnected, and the DGs continue to supply the local load [4]. In this regard, there is a phase between the GC and SA modes where the load voltage is only controlled by the DG and not maintained by the grid. Therefore, the load voltage performance may worsen during this transitional period. To this end, the inverter control must be capable of working during the GC and SA modes and guarantee seamless switching between the two modes [5]. Indeed, these are the essential challenges for switching operations that must be carefully addressed.

The literature on the transition phenomena between the MG operation modes shows that a variety of approaches have been applied to guarantee a smooth transfer between these two modes [6–8]. For instance, the concept of switch-system-based PI linear controls that use a static switch to pass the control loop when the mode of operation changes has been adopted [9]. An approach for smooth transfer using an indirect current control strategy was investigated in [10]. A feed-forward load current for a weak grid was proposed to ensure a seamless transfer, as reported in [11]. A hybrid control approach that combined the integral sliding mode and backstepping technique has been described to enable flexible switching between the SA and GC modes, with an excellent performance and efficiency [12]. In [13], the author argued that a staircase-based frequency variation approach performed with a PI controller efficiently minimized the overall harmonic distortion (THD). Nevertheless, a flexible control technique has been devised to govern the active and reactive powers in the GC mode and the voltage and frequency in the SA mode for single-phase energy routers working in a smart community environment [14]. Therefore, a proportional resonant (PR)-based control technique for indirect current regulation has been adopted to solve the problem of undesired transients in the transition instant [15]. Even though the sliding mode controller in the hybrid renewable energy system has solved the PI controller's problem, the controller's response time is slower under grid voltage distortion in the GC mode and a balanced load or unbalanced load in the SA mode [16]. To this end, a highly hierarchical control model was implemented in [17] to solve the drawbacks of the previous control approaches. The voltage controller was developed with changeable structural parts for voltage disturbance reduction; it tended to make use of the power-sharing capabilities of a droop control. However, the adjustable component process represented system-wide harmonics and delayed the transient responsiveness. Furthermore, a sliding mode control was established to solve the tracking control problem for a bidirectional converter in an aircraft system [18]. Therefore, the authors in [19] proposed an approach based on model predictive control (MPC) to reduce the transient response time. It produced a consistent result that is both simple to construct and inexpensive to execute; however, it suffers from high computation burdens.

On the other hand, most of the reported control techniques require information about the inductor current, load current, and output voltage in order to perform current–voltage exponential monitoring. Recent research on sensorless control solutions using the state observer approaches has been developed to enhance the stability and decrease the number of sensors. In addition, it has been shown that observers are efficient at adjusting for delays within digital control and can estimate measurements with finite analytic tools and procedures without the requirement of sensor communities. A Luenberger observer was built in [20] to enable stable control using inductor current estimates for the SA mode. In addition, in order to enhance the stability and transient efficiency of the inverter under nonlinear load circumstances, an effective nonlinear controller based on a state-feedback observer has been presented for output voltage monitoring [21]. Furthermore, to ensure a smooth transition between both modes, a disturbance observer-based feedforward method has been adopted by storing the estimate of the change in the inner current loop's reference [22].

Additionally, a current sensorless control scheme based on a modified VSG technique has been proposed for single-phase microgrid applications [23]. It has reduced the inductor's current sensor with a seamless transfer capability. A current control technique fitted to a state and disturbance observer (SDO) was used in a recent paper by [24] to address the unknown disturbance issue in an LCL-type single-phase grid-connected inverter. This technique has reduced the influence of external perturbations on the observer's ability to make precise estimations.

Despite the reported control methods achieving rapid and effective synchronization and disconnection, they performed this with limitations. Moreover, the majority of the literature encountered problems, owing to voltage and frequency deviations above the set limitations in transient situations.

In this regard, the present study provides an advanced control method for ensuring a seamless transition while maintaining all of the relevant parameters under supervision, in order to address the shortcomings of the transition process. The following points serve as inspiration for the suggested control:

- The design of an ST-SMC for a three-phase inverter to provide a proper and seamless transition from the grid-connected mode to islanded mode.
- The adoption the digital Luenberger observer (DLO) to estimate the inverter-side current of the system under study will reduce the prep time of the disconnected controller.
- The achievement of a quicker and more effective grid synchronization without losing the phase-angle and frequency stability in both the GC and SA modes.
- A PIL validation to assess the proposed transition technique's efficiency during the GC and SA modes.

The remainder of the work is structured as follows: in Section 2, the proposed transition technique for a three-phase inverter operating in the GC and SA modes is described, including the mathematical model in both modes. The proposed current sensorless control based on the Luenberger observer for the inner current loop is provided in Section 3. In addition, the designed super-twisting sliding mode controller for the outer loop in the SA mode is described in this section. In Section 4, the simulation results and PIL validation are presented. Finally, Section 5 concludes the paper.

2. Structure of Three-Phase VSI Operating in GC and SA Modes with the Proposed Controller

One of the major drawbacks during grid-side anomalies, according to grid standards, is the surveillance of the voltage and frequency at the PCC, as well as the supervision of the maneuver of recloses and relays for a faster isolation of the DG from the utility [25]. All these requirements necessitate the system being packed with an effective control mechanism in order to ensure seamless transition control between the two modes, which is considered a significant issue in this research.

Figure 1 shows the schematic diagram of the grid-connected inverter (GCI) and the suggested transition control. As illustrated in this figure, a three-phase inverter with an LC filter is connected to the utility grid and a three-phase parallel RL load via line impedance. In addition, a DC source is considered as a micro source for generating power via an ideal voltage source inverter (VSI). Furthermore, at the grid side, a static transfer switch (STS) is employed to accomplish the GC and SA operations when islanding happens. In this configuration, the DG works as a current source during a GC operation and then switches to a voltage source to maintain the desired voltage during islanding operations.

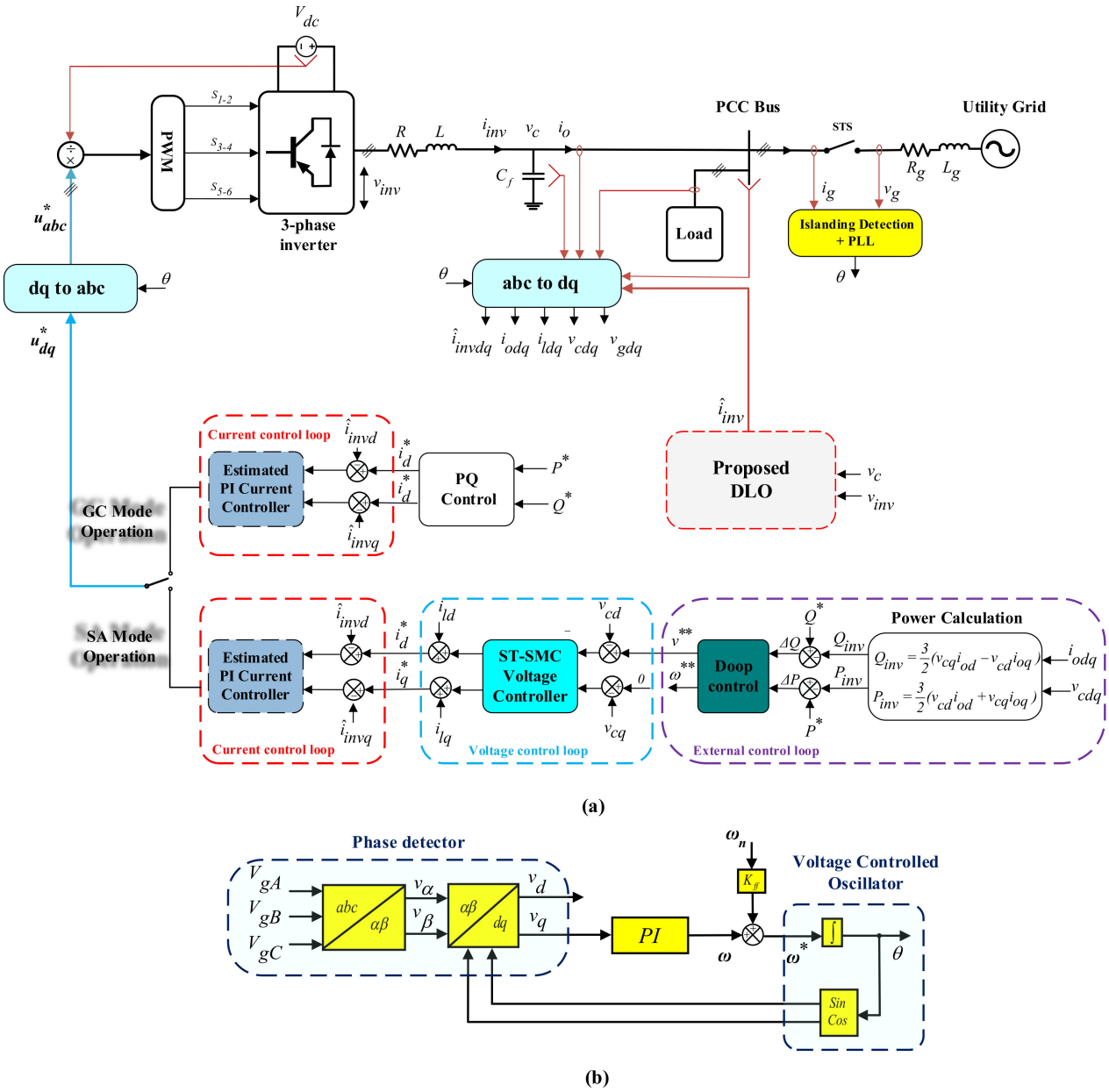

Figure 1. Schematic diagram of: (**a**) a three-phase grid-connected with the proposed control scheme; and (**b**) synchronization algorithm.

The proposed control scheme is accomplished through four key processes, which can be classified as:

- A digital Luenberger-observer-based-estimation of the inverter-side currents, i_{inv}, which adopts the capacitor actual voltage, v_c, and the inverter-side voltage, v_{inv}, as inputs.
- The regulation of the estimated current in the dq frame, $\hat{i}_{invdq}$, to the current references, i^*_{dq}, generated by a power controller according to the desired real and reactive powers (P^* and Q^*). This current control mode is considered for the case of the GC mode of operation.
- Under SA operation, a voltage control mode is adopted, in which the dq capacitor voltages, v_{cd} and v_{cq}, are adjusted to the voltage reference, v^{**}, provided by the droop control and zero, respectively. This adopted control scheme includes a droop controller with a power calculation unit and a double-loop inner controller, which includes an

internal sensorless current controller based on a PI compensator and an outer voltage control loop based on a super-twisting controller. The super-twisting-based-voltage control is needed to keep the system stable and the performance adequate at the transition instant when the grid parameters vary.

- A phase-locked loop (PLL) synchronization algorithm is required to synchronize the output inverter with the utility grid, as seen in Figure 1b. This stage should be capable of extracting and adjusting the frequency of the output inverter.

The resulting duty cycle from dividing the voltage references provided by the current controllers, u^*_{abc}, by V_{dc} is then fed into a PWM, which creates the inverter switches' commands. More details about each block within the proposed control scheme for both the GC and SA modes will be explained in Section 3. Note that "*" refers to a signal reference.

Modelling of the System under Study

In order to establish the state-space representation of the three-phase system given in Figure 1 for both the GC and SA modes, Figure 2 depicts a simplified design. Based on this figure, the equations that define the system dynamic are given as follows:

$$\begin{cases} v_{inv.abc} = Ri_{inv.abc} + L\frac{d}{dt}i_{inv.abc} + v_{c.abc} \\ i_{inv.abc} = C_f\frac{d}{dt}v_{c.abc} + i_{o.abc} \\ i_{o.abc} = i_{l.abc} + i_{g.abc} \end{cases} \quad (1)$$

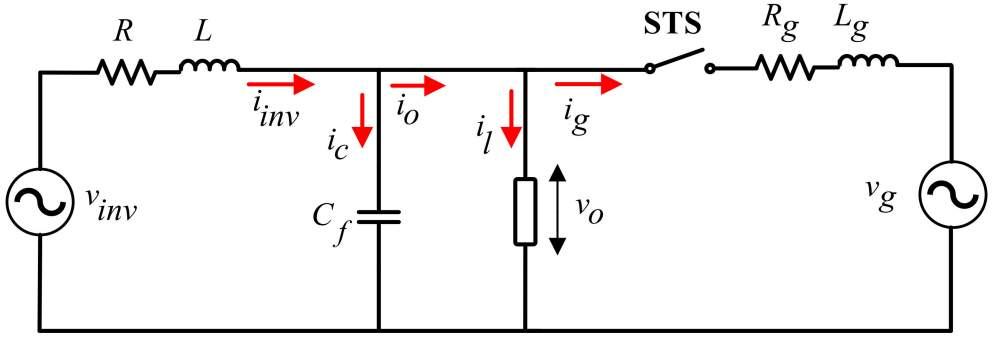

Figure 2. Basic structure of a three-phase grid-connected inverter.

In addition, (1) can be rewritten as follows:

$$\begin{cases} L\frac{d}{dt}i_{inv.abc} = v_{inv.abc} - v_{c.abc} - Ri_{inv.abc} \\ C_f\frac{d}{dt}v_{c.abc} = i_{inv.abc} - i_{o.abc} \end{cases} \quad (2)$$

where $v_{inv.abc}$ is the output voltage of the inverter at each phase and $i_{inv.abc}$ and $i_{o.abc}$ are the three-phase inverter output current and the inverter output filter current, respectively. $v_{c.abc}$ indicates the capacitor voltage, C_f is the filter capacitor, and L and R are the filter inductor and resistor, respectively. $i_{l.abc}$ and $i_{c.abc}$ are the load current and capacitor currents. $i_{g.abc}$ defines the grid current.

By applying the parck's transformation given in Equation (3) below, the mathematical model of the GCI in the synchronous reference frame (SRF) can be expressed by (4).

$$\begin{bmatrix} x_d \\ x_q \end{bmatrix} = \frac{2}{3}\begin{bmatrix} cos\theta & cos(\theta - \frac{2}{3}\pi) & cos(\theta + \frac{2}{3}\pi) \\ -sin\theta & -sin(\theta + \frac{2}{3}\pi) & -sin(\theta - \frac{2}{3}\pi) \end{bmatrix} \times \begin{bmatrix} x_a & x_b & x_c \end{bmatrix}^T \quad (3)$$

$$\begin{cases} \frac{di_{invd}}{dt} = \frac{1}{L}(v_{invd} - v_{cd}) - \frac{R}{L}i_{invdq} + w.i_{invq} \\ \frac{di_{invq}}{dt} = \frac{1}{L}(v_{invq} - v_{cq}) - \frac{R}{L}i_{invdq} - w.i_{invq} \\ \frac{dv_{cd}}{dt} = \frac{1}{C_f}(i_{invd} - i_{od}) - w.v_{cq} \\ \frac{dv_{cq}}{dt} = \frac{1}{C_f}(i_{invq} - i_{oq}) + w.v_{cd} \end{cases} \quad (4)$$

where $v_{inv.dq}$ and $i_{inv.dq}$ indicate the inverter output voltage and current in the dq frame and $v_{c.dq}$ and $i_{o.dq}$ are the dq capacitor voltage and output current components, respectively. ω defines the angular speed.

3. Proposed Control Scheme for Both GC and SA Modes of Operation

This section's goal is to precisely explain the adapted control technique for the GCI under investigation, which is shown in Figure 1. As previously mentioned, the DG inverter can operate in either the GC mode or SA mode. Under typical grid situations, the DG inverter functions in the GC mode and aids in delivering the load. Moreover, an STS allows the DG to switch to the SA mode in the event of an abnormality or problem happening. Specifically, when transferring between the two modes, the transfer must be achieved without a transitional state and the load should not be severely impacted. To overcome this in the GC mode, an effective current sensorless-control-based Luenberger observer is developed to achieve the excellent tracking of the inverter-side current and a high resistance against parametric fluctuations and disturbances. On the other hand, a super-twisting sliding mode controller is designed for the SA operating mode to guarantee the challenges that will be explained in this paper.

3.1. Proposed Current Sensorless Control for GC Operating Mode

Under normal operation and conditions, the STS is closed. The DG sends the generated power to the load and utility, such as the grid-side parameters, which are set by the utility. A proposed strategy based on an SRF is depicted in Figure 3a–c. It is made up of an outer loop PQ controller, an inner loop current controller, and the proposed digital Luenberger observer. Moreover, the synchronization concept is accomplished by the SRF PLL, as shown in Figure 1b.

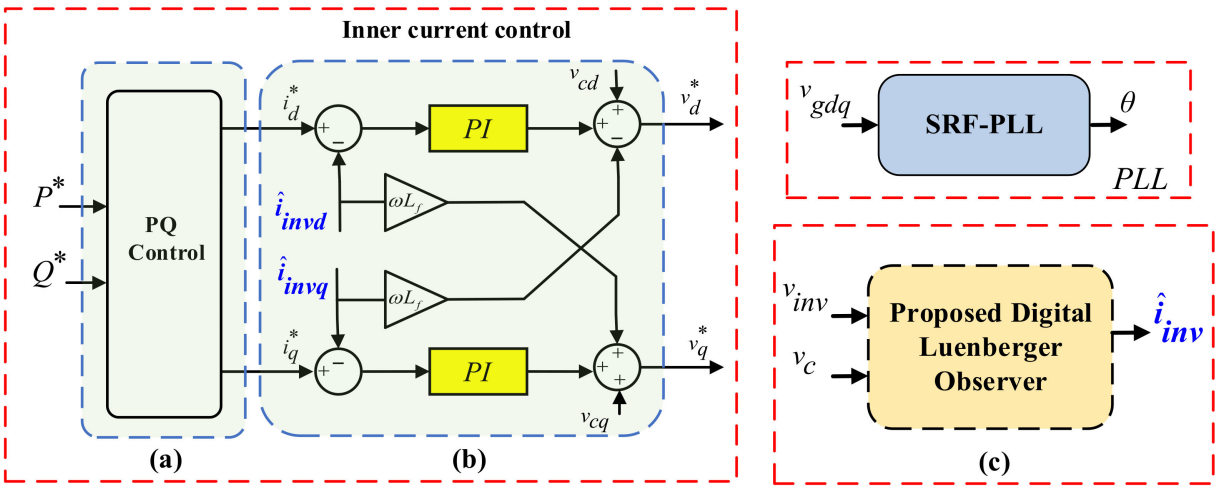

Figure 3. Control structure for the grid-connected operation: (**a**) PQ control; (**b**) inner current control; and (**c**) proposed digital Luenberger observer.

This approach consists of generating a reference of active and reactive power components using the PQ outer loop controller. It also permits obtaining the values of i^*_{invd} and i^*_{invq}, which are the inner loop's inputs. (P^*, Q^*) represent the references for the active and reactive power, respectively. For regulating the inner current loop, an estimated current PI controller is adjusted in the *dq* axes with feed-forward decoupling, supplied by comparing i^*_{invdq} with the *dq* estimated components, which are generated by using the Luenberger observer $\hat{i}_{invdq}$, respectively. This allows for obtaining the inverter voltage references, v^*_d and v^*_q, which are transformed into three-phase voltages through a *dq*-abc transformation. Consequently, the abc voltages are delivered to the PWM-generating block, which produces the commands of the inverter's switches, to ensure the inverter's control functionality, as well as an effective power supply [26].

3.1.1. Digital Luenberger Observer

As previously stated, to decrease the operational complexity and system cost of the typical model under study, a digital Luenberger observer (DLO) is proposed, without communication and measurement sensors by estimating the inverter-side current, which must be controlled in this case. A DLO is well suited for the case of the GC mode and the sudden transfer from the GC to SA operation mode, due to the strong durability features of parameter changes and external disturbances [27]. The system's observability should be studied before developing the DLO.

Construction and Observability Analysis of DLO

The planned control needs a measurement of the inverter inductor's current, as shown in Figure 1. For this reason, a DLO is designed to estimate the inverter output current by considering the variables i_{inv} and v_c to be the system variables. (1) and (2) are given in continuous time as follows:

$$\begin{cases} \frac{d}{dt}x(t) = Ax(t) + B.v_{inv}(t) \\ y(t) = Cx(t) \end{cases} \tag{5}$$

where $x(t) = [v_c(t) \quad i_{inv}(t)]^T$, A, B, and C are defined as follows:

$$A = \begin{bmatrix} 0 & \frac{1}{C_f} \\ \frac{-1}{L} & 0 \end{bmatrix},\ B = \begin{bmatrix} 0 & \frac{-1}{C_f} \\ \frac{1}{L} & 0 \end{bmatrix},\ C = [1 \quad 0] \tag{6}$$

The system's observability matrix is described by (7):

$$rank = [C \quad CA]^T = 2 \tag{7}$$

According to Equation (7), the rank of the matrix is complete. Consequently, the system is observable. The following equation represents a dynamic Luenberger observer:

$$\begin{cases} \dot{x}(t) = A.\hat{x}(t) + B.u(t) - G(\hat{y}(t) - y(t)) \\ \hat{y}(t) = C.\hat{x}(t) \end{cases},\ G = [G_1 \quad G_2]^T \tag{8}$$

The observation error is illustrated as $e = (\hat{y} - y)$. The terms G_1 and G_2 are the observer gains and the superscript "^" represents the estimated value. Moreover, the digital structure of the suggested Luenberger sensorless current is derived via the Euler technique.

$$\begin{cases} \hat{x}_{(k+1)} = A_k.\hat{x}_{(k)} + B_k.u_k + G_k(\hat{y}_{(k)} - y_{(k)}) \\ \hat{y}_{(k)} = C_k.\hat{x}_{(k)} \end{cases} \tag{9}$$

This considers $e_{(k)} = (A_k - G_k.C_k)(\hat{x}_{(k)} - x_{(k)})$ to be the error of the state vector, where C_k is the control matrix and G_k is the gain matrix. The conceptual description of the DLO is shown in Figure 4.

The resultant equation may be described as (10):

$$\begin{cases} \dot{v}_{c(k+1)} = G_1.T(y_{(k)} - \hat{y}_{(k)}) + \dot{v}_{c(k)} + \frac{T}{C_f}(i_{inv(k)} - \hat{i}_{o(k)}) \\ \hat{i}_{inv(k+1)} = G_2 T(y_{(k)} - \hat{y}_{(k)}) + \hat{i}_{o(k)} \end{cases} \quad (10)$$

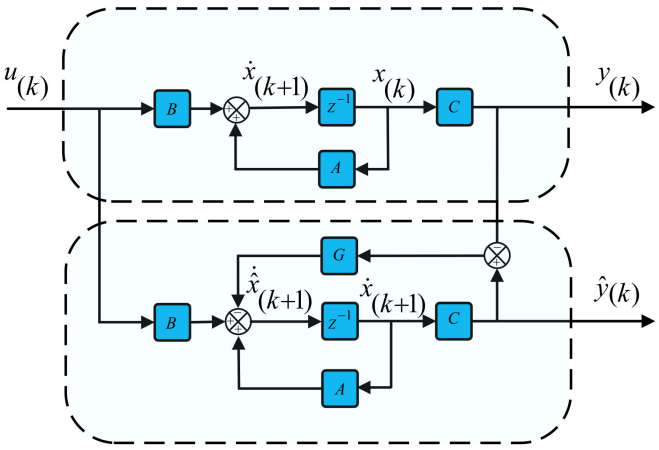

Figure 4. Conceptual description of the DLO.

Observer Gain Design

For designing the state observer, a necessary condition in finding the estimator gains A and B in (9) through a practical decision can accomplish the stability of the observer and the state error vector's dynamic. The selection of this matrix checks if the eigenvalues β_i of $(A_k - G_k.C_k)$ are located in the left half-plane of a unit circle, which is denoted and defined as $|\beta_{i=1.....n}|\langle 1$. Hence, as reported by [28], this can be located at the poles observed in the Z domain as follows:

$$(zI - A_k + H_k.C_k) = (z - \beta_1)(z - \beta_2)\ldots(z - \beta_n) \quad (11)$$

3.2. Proposed Control Scheme Based on a Super-Twisting Algorithm for SA Mode

Fault detection, otherwise defined as islanding detection, is a significant issue in this application. When an islanding condition occurs, the STS is deactivated. The load fluctuates and must be isolated from the utility grid. In this case, voltage and frequency regulation with power sharing should be constantly considered. Therefore, the V/f controller is employed as the voltage control through the droop control technique.

Under the V/f controller, a flexible control that includes the regulation of the active and reactive power is employed to keep a consistent power delivery to the load. As illustrated in Figure 5, a hybrid control is designed using voltage and current loops. The droop control is primarily responsible for setting the correct references upon grid disconnection, when the reference voltages on the dq axes are v^{**} and zero, respectively.

Additionally, a super-twisting sliding mode controller, which will be detailed in the next section, is fed as a voltage control by measuring the difference between v^{**} and v_{cd}. Furthermore, the resulting control is compensated with i_{ldq} to obtain the inputs for the current loop. In order to regulate the estimated inverter-side currents, $\hat{i}_{invdq}$, inner current loops are considered. It is worth mentioning that the inner loops' dynamics are considerably quicker than the voltage loops.

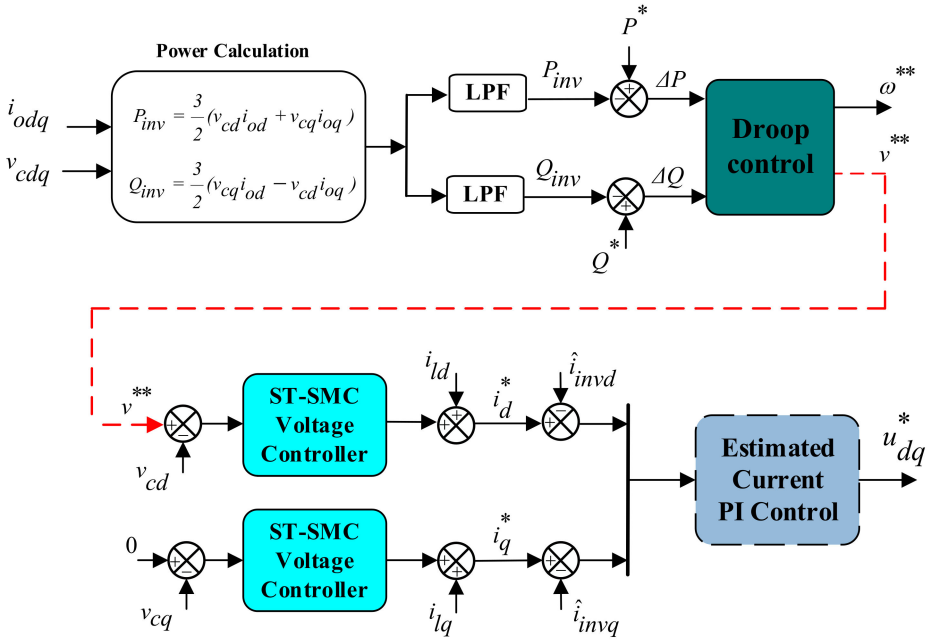

Figure 5. Control structure for the SA operation.

3.2.1. Droop Control Strategy

In the case of an islanding mode, the droop control is employed to share the load requirement, in order to guarantee the stable microgrid operation. Hence, during this operation mode, the inverter should be capable of regulating the output voltage and frequency by detecting the fluctuations in the reference and value measurements [29]. It can calculate the active P_{inv} and Q_{inv} reactive power from the (v_{cd}, v_{cq}) and (i_{od}, i_{oq}), which are sensed and changed locally. In Equation (11), the formula for calculating P_{inv} and Q_{inv} is defined as follows:

$$\begin{cases} Q_{inv} = \frac{3}{2}(v_{cq}i_{od} - v_{cd}i_{oq}) \\ P_{inv} = \frac{3}{2}(v_{cd}i_{od} + v_{cq}i_{oq}) \end{cases} \quad (12)$$

The references generated by the droop control method are achieved using Equation (13).

$$\begin{cases} v^{**} = -n.\Delta Q \\ \omega^{**} = -m.\Delta P \end{cases} \quad (13)$$

As n and m represent the droop coefficients, the method is often designed in inverse proportion to the DG unit rating to share the load requirements in proportion to its power rating [30].

3.2.2. Outer Loop Voltage Regulation Based on Super-Twisting Algorithm

In an AC microgrid inverter operation, the DG inverter control should be resistant to parameters and external disturbances, in order to maintain the system's reliability and efficiency. In contrast, the process is abrupt and unpredictable during an islanding scenario. In this case, the controller must take quick action to limit harm to the system.

This section explains how the proposed control should start preparing the DG for disconnect in the event of an islanding situation. The process for disconnection is equipped with a robust ST-SMC voltage control to achieve a seamless transfer between the GC and SA modes. The super-twisting algorithm (STA) is one of the major frequently applied nonlinear approaches for DG inverter operation control, owing to its adaptability and the simplicity of its application. The ST-SMC is well-suited for real-world applications because it is less susceptible to small perturbations in the output and potential errors [31]. When

compared to the conventional SMC approach, the STA algorithm reduces chattering issues. The control consists of two portions, u_1 and u_2, as defined by [32] in Equation (15).

$$U_{st} = u_1(t) + u_2(t) \tag{14}$$

with

$$\begin{cases} u_2 = -\lambda |S|^r sign(S) \\ \dot{u}_1 = -\alpha sign(S) \end{cases} \tag{15}$$

where λ and α represent the control gains required to build a successful ST-SMC [33]. To preserve the stability, the nonlinearity can be adjusted by altering the coefficient r. It must be positive and have a value between 0 and 0.5. ST-SMC employs simple information about S and does not need to evaluate the sign of $\dot{S}$. The ST-SMC's structural design is illustrated in Figure 6.

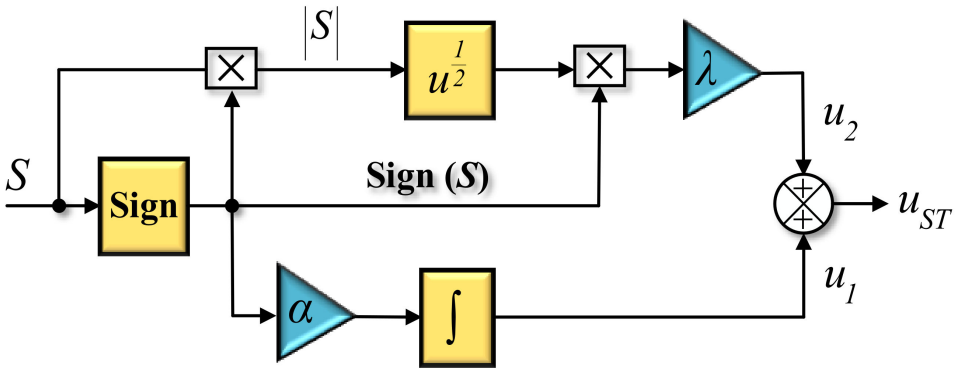

Figure 6. The super-twisting control trajectory's block design.

The sufficient requirements for limited time convergence are presented in [34], as presented in (16):

$$\begin{cases} \alpha > \frac{\Phi}{T_M} \\ \lambda \geq \frac{4\Phi T_M(\alpha+\Phi)}{T_m{}^3(\alpha+\Phi)} \end{cases} \tag{16}$$

α, λ, Φ, and T_M represent the positive constants. Φ is defined as a positive bound for the undefined function ϕ, while T_M and T_m are the positive lower and upper limits of the unknown variable γ at the second derivative of the sliding surface, provided by [35].

The proposed stability analysis in [36] can be shown using an appropriate candidate Lyapunov function V, as defined by:

$$V = \alpha |S| + \frac{1}{2} S^2 \tag{17}$$

As a factor of unknowns such as changing parameters, perturbations, and measurement errors, the rule for a system with a disturbance can be stated as follows:

$$\dot{x} = ax + bu + k \tag{18}$$

where x and u define the state vector and the input, respectively, assuming that the system disturbance is constrained, and k represents the disturbance, as defined in the equation below:

$$k \leq k_{max} |S|^{0.5} \tag{19}$$

The Lyapunov function's time derivative can be expressed as follows:

$$\dot{V} \leq \alpha sign(S) \left(-\lambda |S|^{0.5} sign(S) + k_{max} |S|^{0.5} \right) \tag{20}$$

By selecting k_{max}, this gradient is negative and certain for the system to be asymptotically stable.

An ST-SMC is explored to regulate the dq axis for the outer loop voltage based on the following sliding surface equations:

$$\begin{cases} S(v_{cd}) = v_{ref-d} - v_{cd} \\ S(v_{cq}) = v_{ref-q} - v_{cq} \end{cases} \tag{21}$$

where v_{ref-dq} are the voltage references generated by the droop control, as mentioned previously, and v_{cdq} are the capacitor voltages in the dq-frame. The block diagram of the outer loop voltage regulation is illustrated in Figure 7.

$$\begin{cases} i_{dq}^{*} = -\lambda_{v_{c-dq}} \left| S(v_{c-dq}) \right|^{r} signS(v_{c-dq}) + u_1 + i_{ldq} \\ \dot{u}_1 = \alpha_{vc-dq} signS(v_{c-dq}) \end{cases} \tag{22}$$

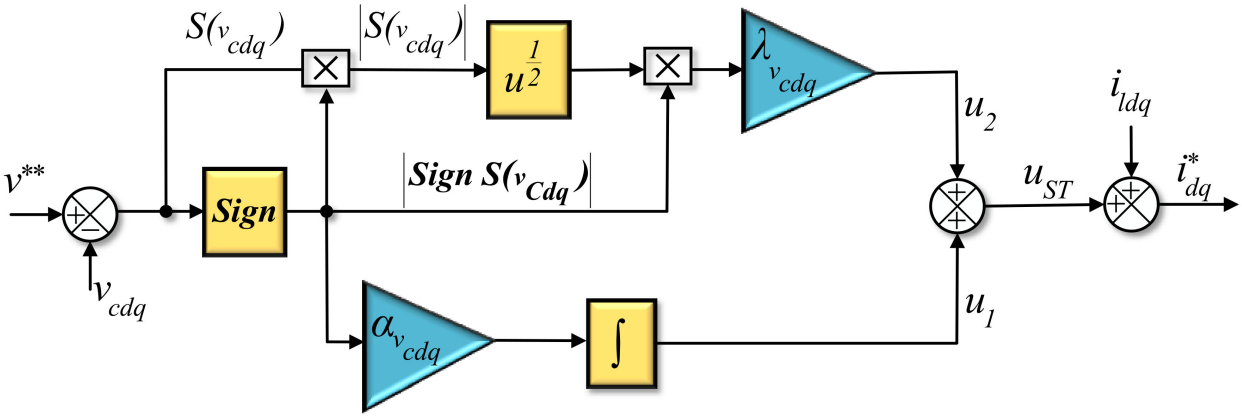

Figure 7. Block diagram of the outer loop voltage regulation.

Supported by past analysis, the voltage reference in the SA mode can be mathematically represented as:

$$\begin{cases} u_d^{*} = (k_p + \frac{k_i}{s})(i_d^{*} - i_{invd}) - (w_o L_1 . \hat{i}_{invq}) + v_{cd} + \lambda_{v_{cd}} |S(v_{cd})|^{r} signS(v_{cd}) + u_1 + i_{ld} \\ u_q^{*} = (k_p + \frac{k_i}{s})(i_q^{*} - i_{invq}) - (w_o L_1 . \hat{i}_{invd}) + v_{cq} + \lambda_{v_{cq}} |S(v_{cq})|^{r} signS(v_{cq}) + u_1 + i_{lq} \end{cases} \tag{23}$$

4. Simulation Results and PIL Validation

To demonstrate the efficacy of the control mechanism proposed in this section, specifically for establishing a seamless mode transfer from the GC to SA mode, a comparative test with the classical transfer approach is addressed using PSIM software. The simulation results are developed under a PIL test in quasi-real time to assess the effectiveness of the control scheme.

The estimated gains for the digital Lunenberger observer and the suggested controller parameters are scheduled in Table 1. The planned scenario assumes that the system functions in the GC mode before switching to the SA mode at t = 0.35 s.

Table 1. Power and controller parameters.

Parameters	Specification
DC-link Voltage	600 V
Grid Voltage (RMS)	155.56 V
Switching Frequency	20 kHz
Sampling Time	10 µs
Grid Impedance	0.05/0.0016 mH/mΩ
Load	72.5 Ω + 93.4 mH
Filter Inductor	4 mH
Filter Capacitor	60 µF
Control Gain ST-SMC (α)	12
Control Gain ST-SMC (λ)	3.46
Proportional Gain $\left(k_{pc}, k_{ic}\right)$	$19.6/49.10^3$
Proportional Gain $\left(k_{pv}, k_{iv}\right)$	0.294/10.5

4.1. Simulation Results and Discussion

Figure 8 shows the observer and measured currents on the inverter-side i_{inv}. Evidently, the observed current of the a-phase inductor accurately corresponds with the measured current for the GC and SA modes. The proposed sensorless controller responds with a greater tracking precision and quicker reaction time in both modes. Even though islanding is detected at t = 0.35 s, their dynamic effectiveness is maintained.

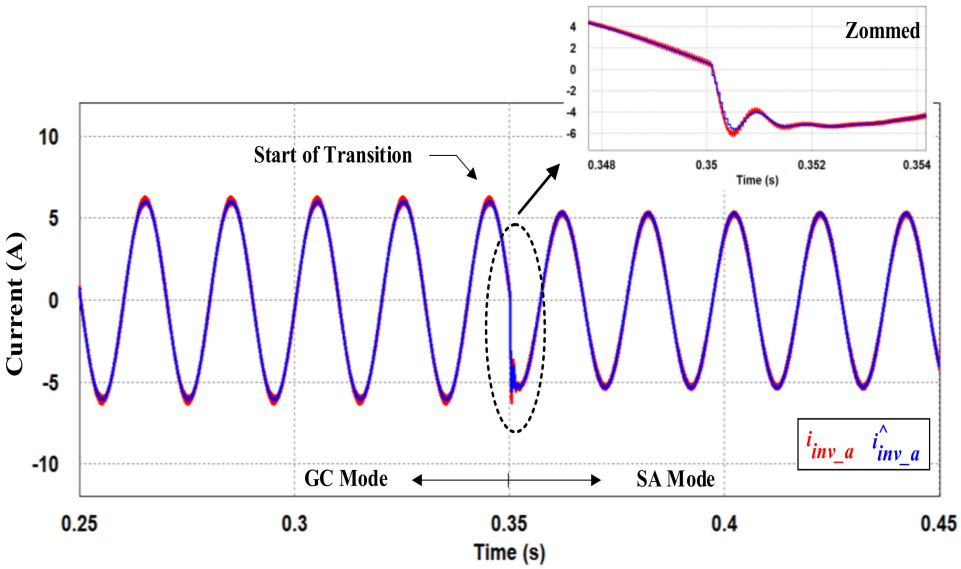

Figure 8. Simulation results of an inverter-side current for phase A and her observed under GC and SA modes with the suggested ST-SMC based on the DLO scheme.

To emphasize the observer's efficiency even further, the three-phase estimated inverter side currents rapidly drop at the transition instant, as shown in Figure 9a,b. In addition, as can be observed, the dynamic tracking performance is superb and there is no tracking loss for the three-phase waveforms during the transition instant, which is approximately without overshooting when the SA mode starts.

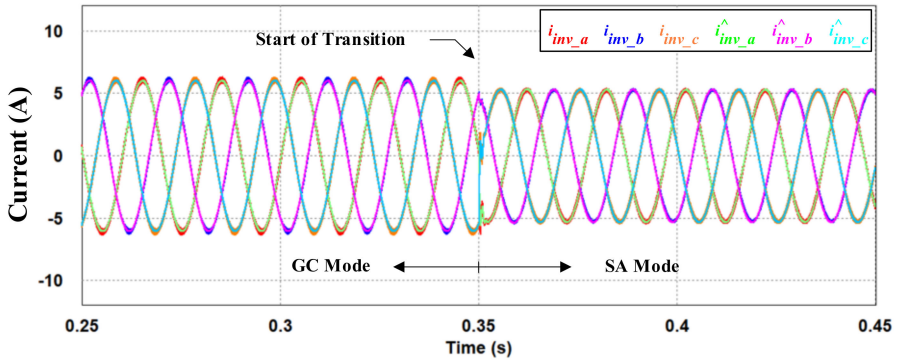

(**a**)

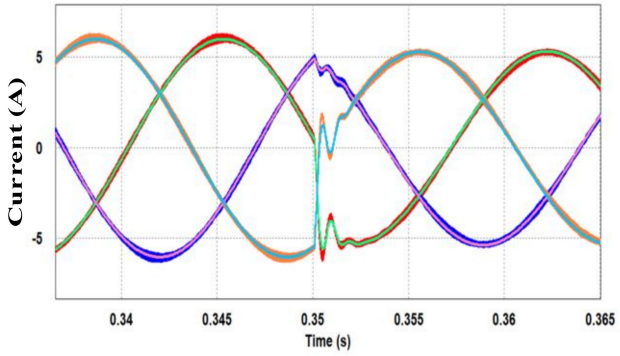

(**b**)

Figure 9. Transition from GC and SA modes: (**a**) three-phase inverter-side currents and their observed with the proposed ST-SMC based on the DLO scheme; and (**b**) zoom in.

The estimated error in both the GC and SA modes is illustrated in Figure 10. This obtained value is extremely small at around 0.1 V, confirming the great estimation accuracy of the suggested Luenberger observer. Evidently, the proposed technique provides a superior steady-state (minimal observation errors) and dynamic performance (reduced settling time).

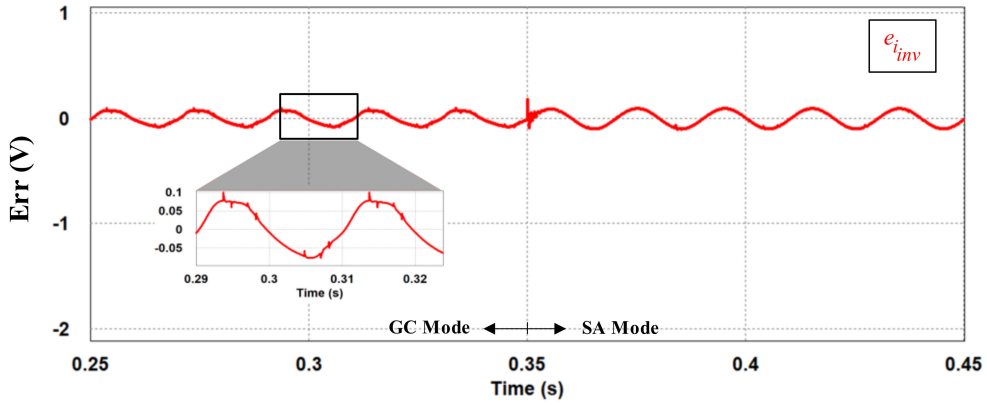

Figure 10. Observation error of inverter-side current for phase A under GC and SA modes.

In Figure 11, the estimated and measured currents of the three-phase inverter-side are depicted separately, evaluating the observer's estimating performance. The comparison clearly demonstrates that the presented controller exceeds the measured one in terms of the quality of its signals, sensitivity, and rapid dynamic response. The proposed method has exceptional harmonic suppression capabilities.

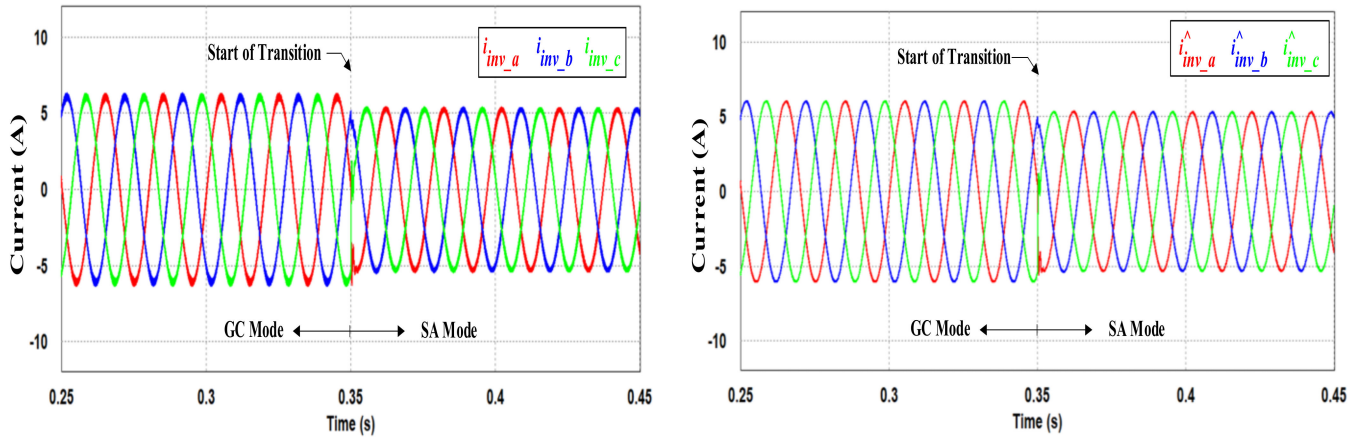

Figure 11. Comparative results for three-phase inverter-side current: (**a**) measured values; and (**b**) estimated value with proposed ST-SMC based on the DLO scheme.

To highlight the robustness of the designed ST-SMC scheme, a comparison with the classical PI controller is conducted and the results are given in Figures 12–14. Figure 12 portrays the system response obtained with the two compared controllers (the classical PI and proposed ST-SMC based on the DLO algorithm) in a specified test scenario. It displays the active powers transferred to the output of the DG system on both the grid and load sides. The suggested control method is less impacted by the transfer between the two modes. The success of the suggested control is shown by the fact that the switching between the two modes has less of an effect on the active powers.

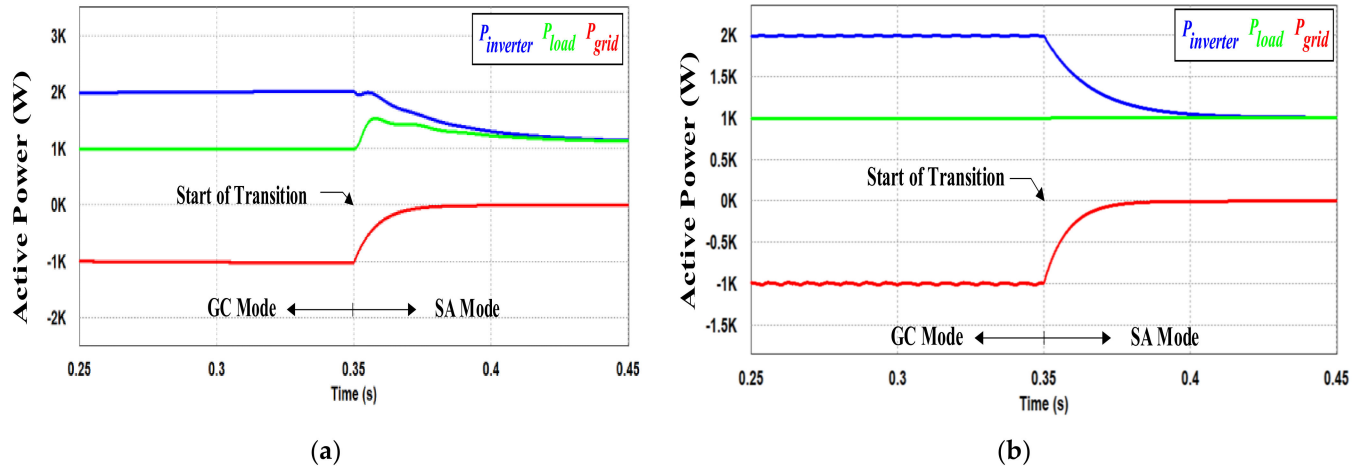

Figure 12. Active power flow simulation results: (**a**) the traditional PI technique; and (**b**) the suggested ST-SMC scheme based on the DLO scheme.

Figure 13 depicts the comparable current response at the local load side $i_{load.abc}$.This result demonstrates that the suggested method reduces the impact of the operation transition from the GC to SA mode on the system.

Figure 14 depicts the load voltage achieved using the two comparative controllers in the suggested test scenario. It illustrates the frequency and temporal responsiveness of the output voltage. In this case, comparing the results of the voltage shows that the suggested control strategy is better at getting rid of disturbances. In order to allow for seamless transitions, the present control considerably improves the quality of the voltage waveform.

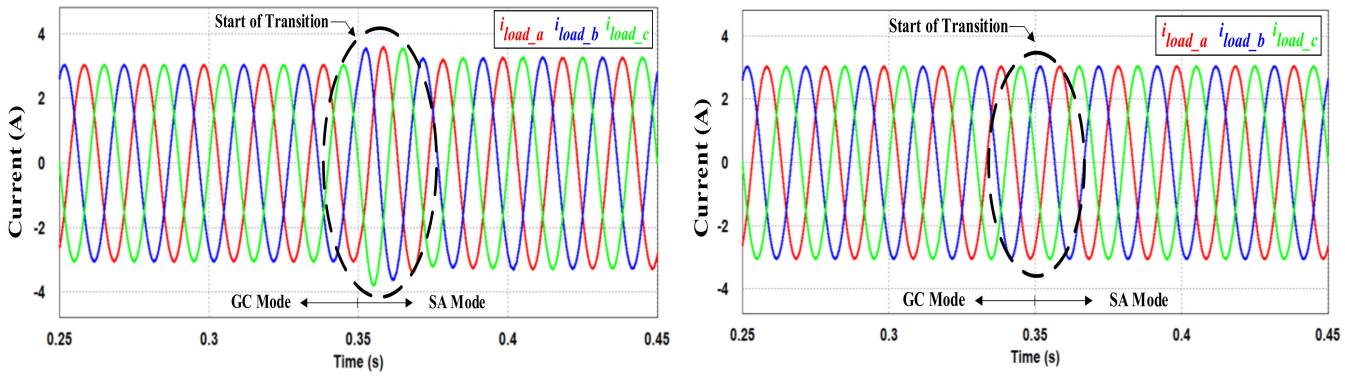

Figure 13. Simulation results of load current: (**a**) the traditional PI technique; and (**b**) the suggested ST-SMC based on the DLO scheme.

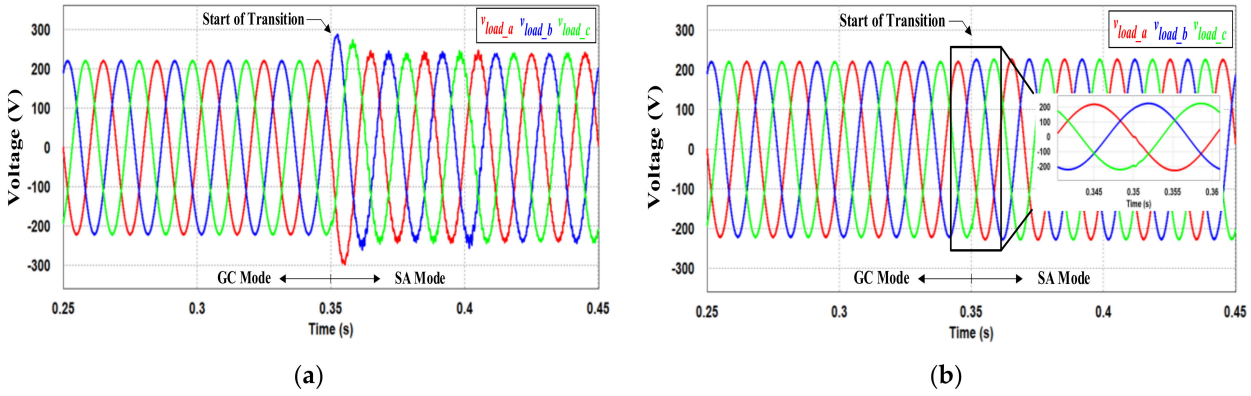

Figure 14. Simulation results of load voltages: (**a**) the traditional PI technique; and (**b**) the suggested ST-SMC based on the DLO scheme.

Figures 15 and 16 show the angle phase and grid frequency extracted by the SRF-PLL under the GC and SA modes. As an effective example of the SRF-PLL's capability, it is evident that the frequency displays an excellent effectiveness and smoothly reacts in a transition instant. Moreover, the phase angle holds constant in both modes, indicating that a system synchronization could successfully develop in the inverter system.

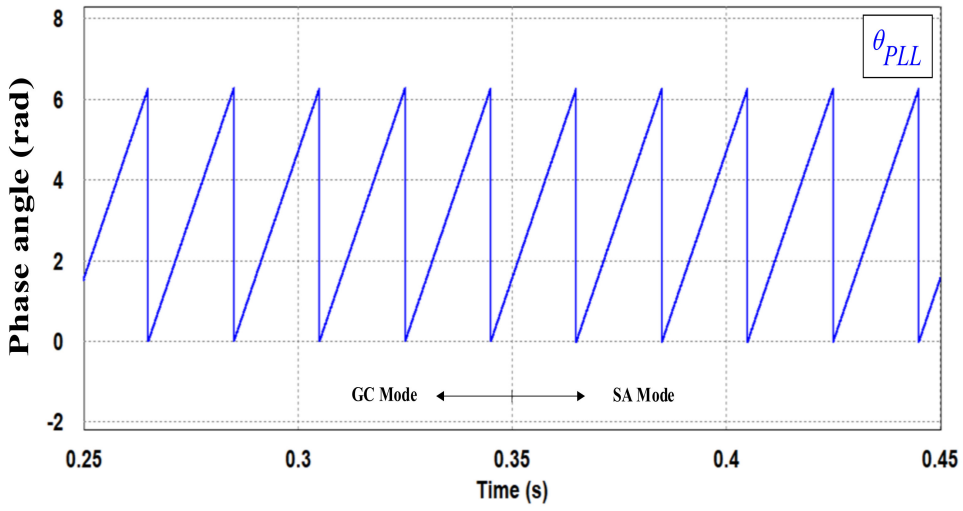

Figure 15. Result of the simulation of phase angle extracting by SRF-PLL under GC and SA modes.

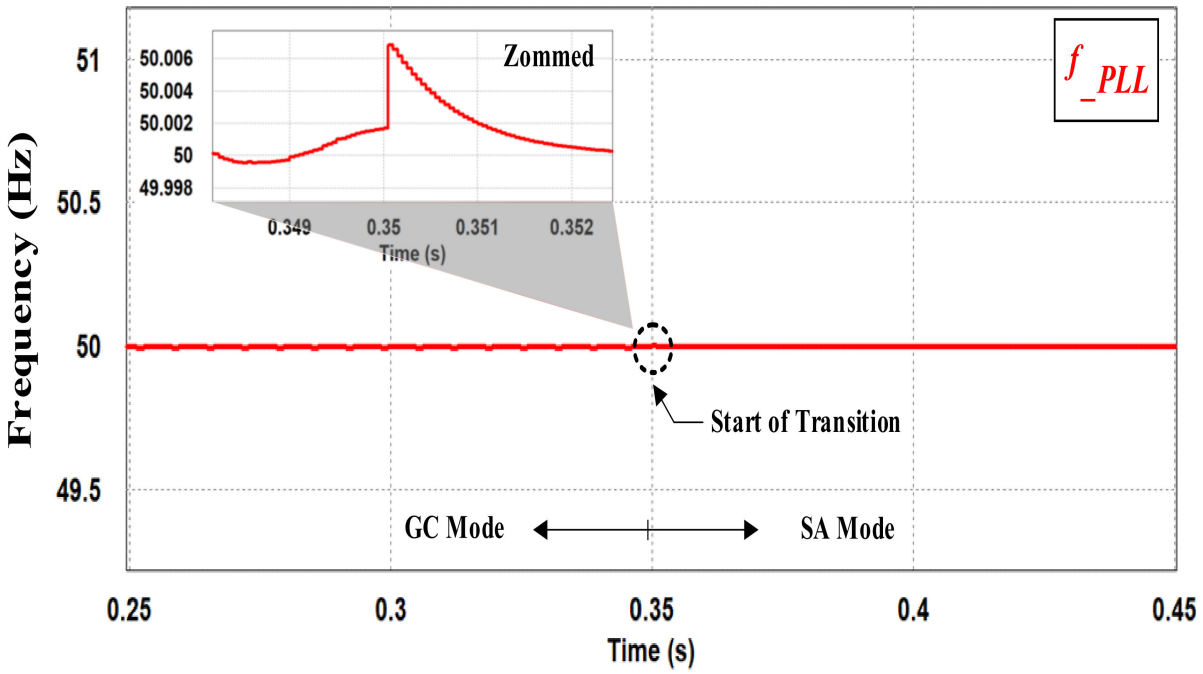

Figure 16. Result of the simulation of frequency extraction by SRF-PLL under GC and SA modes.

4.2. PIL Implementation Using DSP Board TMS32F28335

Leading to outcomes that are precise and close to practical conditions, the processor in the loop (PIL) has steadily emerged as a useful tool for the implementation of converters and regulation in AC microgrids. In a DG inverter operation, some tests are difficult to execute in practice because they need variations in the states of the grid-connected or stand-alone conditions; this is simple to implement in a PIL based on the TMS32F28335 DSP board. In this paper, the effectiveness and achievability of the super-twisting algorithm based on a digital Luenberger current observer are validated using a processor in the loop. Figure 17 depicts the steps for configuring the PIL test using the TMS32F28335 DSP board in the PSIM platform.

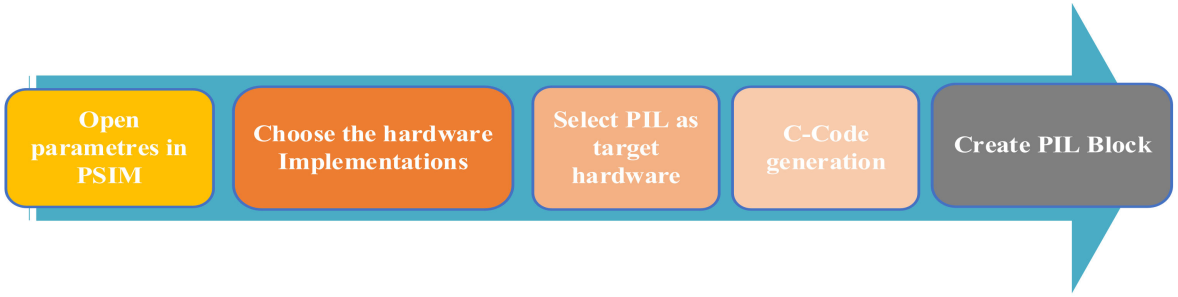

Figure 17. Steps for parameterizing PIL test with DSP board TMS32F2.

The proposed digital control generates a C-code, which is compiled and linked with the code composer studio (CSS), where it is then encoded and executed on the DSP board with a sample time of 40 µs [37]. However, an established PIL block is built in the control structure that integrates the produced code based on the TMS32F28335 DSP board from Texas Instruments.

The co-simulation PIL-based DSP delivers an alternative test stage for controlling and designing an embedded system, with a minimal set of options and a simple implementation. Furthermore, the PIL test system decreases the setup time by demonstrating the validity of the suggested digital control. Figure 18 depicts the hardware implementation of the proposed technique. The PIL tool is regarded as one quasi-real-time method for designing efficient control techniques with a great flexibility [38].

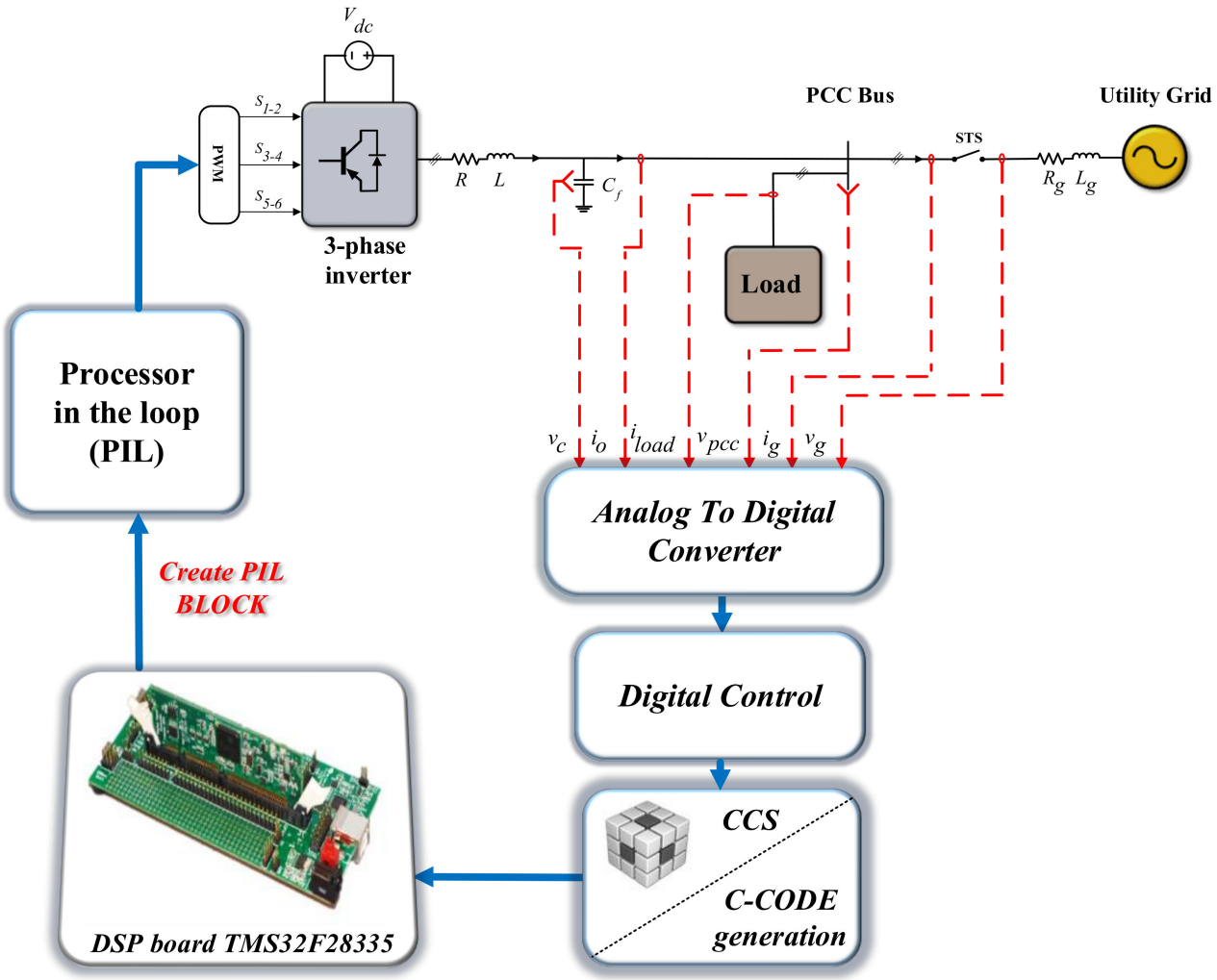

Figure 18. The DSP-based PIL layout implementation of the proposed digital control.

Considering that transitions occur at t = 0.35 s, the same tests are evaluated as those in the PSIM simulations. Figures 19–22 show the obtained results, which highlight the high responses of the load voltages and currents under the GC and SA modes, as well as the voltages and currents of the inverter side and their estimates. In addition, the acquired results demonstrate robust control qualities, including a seamless transition between the MG operating modes, as well as efficacy and resilience throughout both the GC and SA operation modes. From Figure 23, it is clear that the proposed scheme significantly improves the total harmonic distortion (THD) of the voltage waveform, which is reduced from 3.14% with a conventional controller to 0.74% with the proposed technique. Comparing the voltage responses shows that the suggested control strategy has a better ability to minimize disturbances.

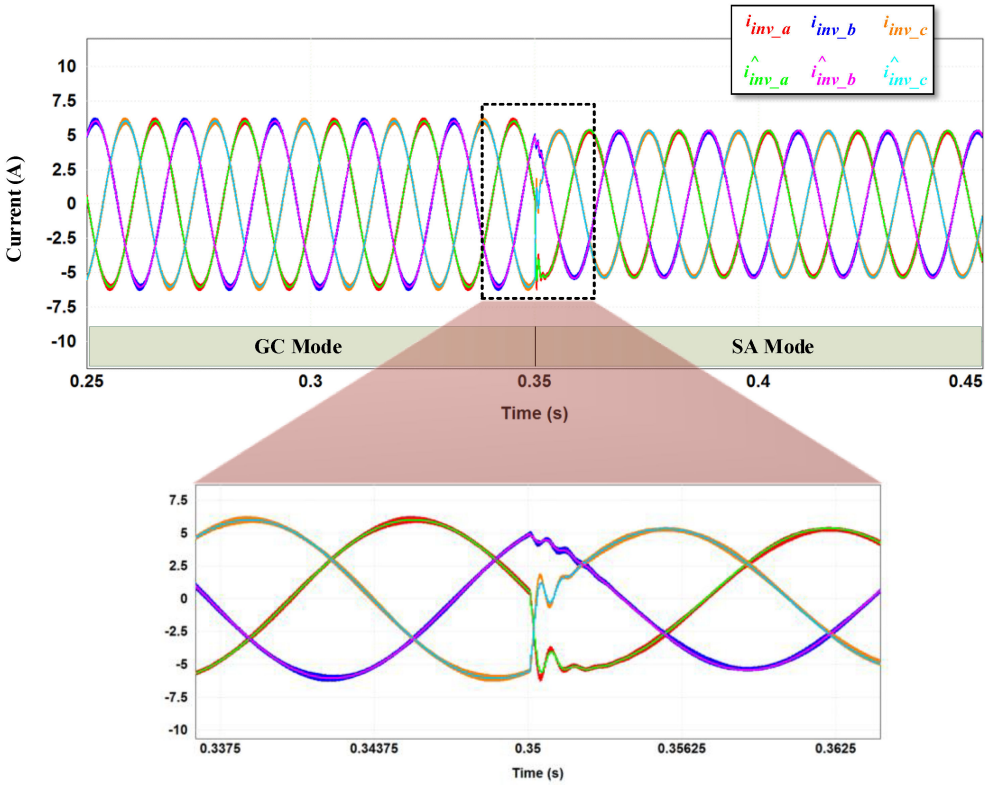

Figure 19. PIL results of transition from GC and SA modes for three-phase inverter-side currents and their observed times with the suggested ST-SMC based on the DLO scheme.

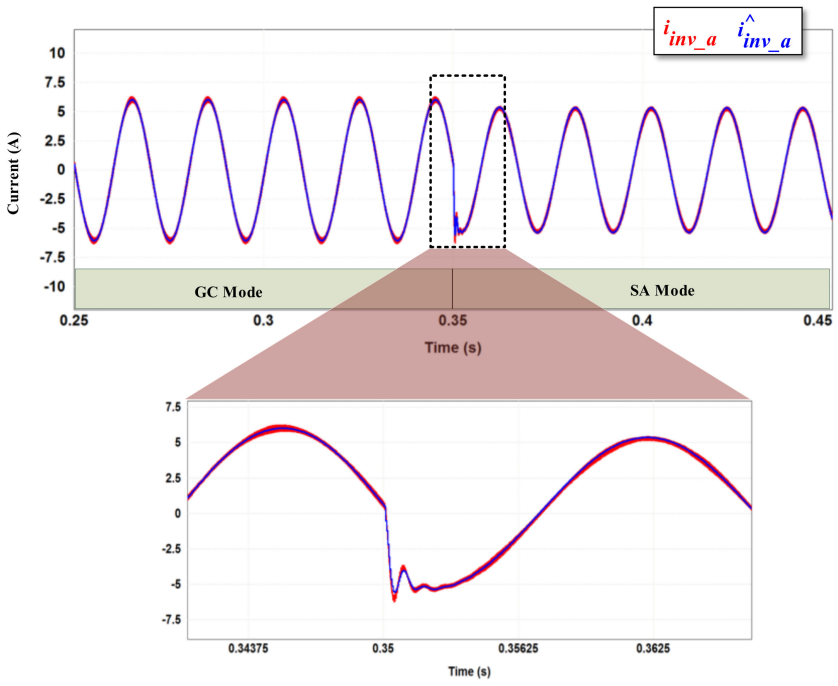

Figure 20. PIL results of an inverter-side current for phase A and her observed under GC and SA modes with the proposed ST-SMC based on the DLO scheme.

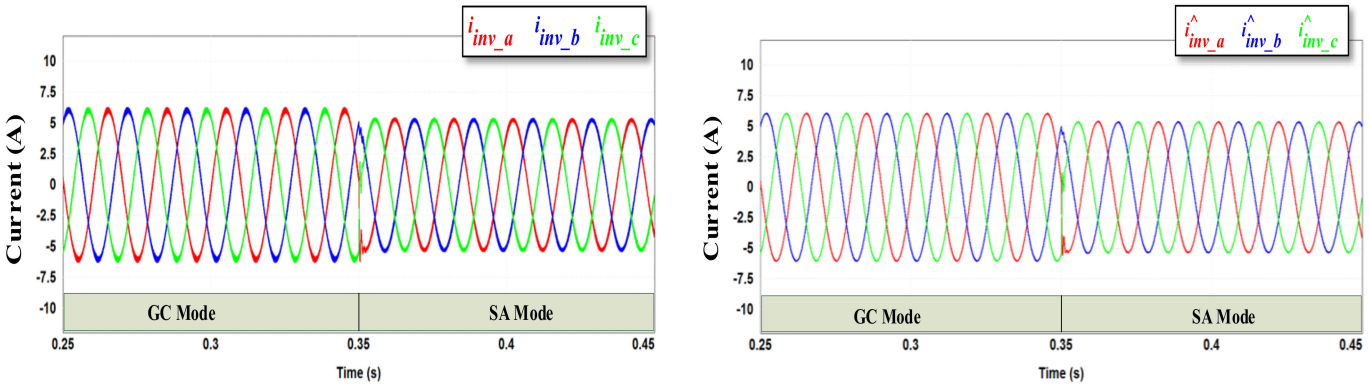

(**a**) (**b**)

Figure 21. PIL results for a comparative test for three-phase inverter-side current: (**a**) measured values; and (**b**) estimated value with the proposed ST-SMC based on the DLO scheme.

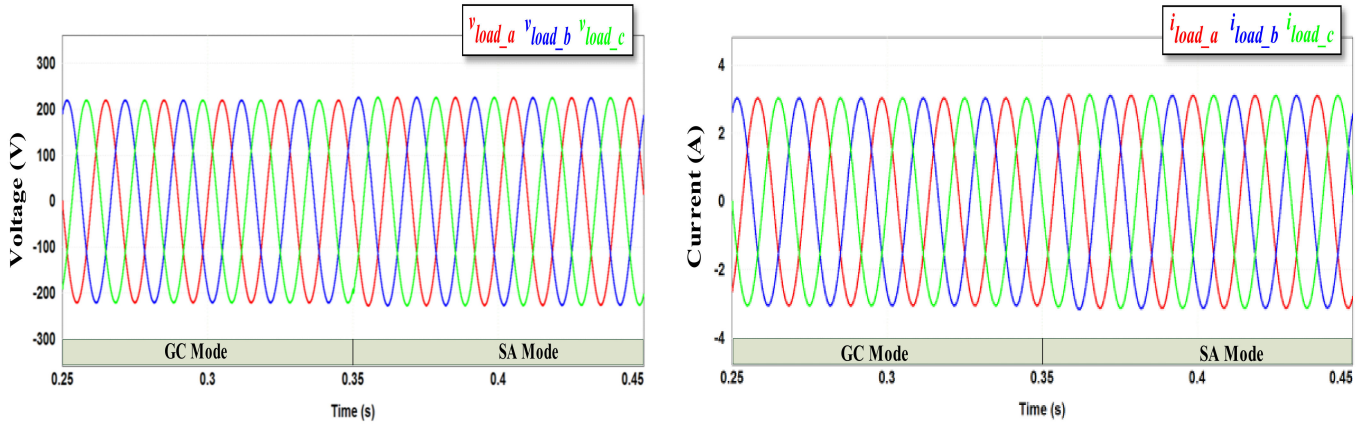

(**a**) (**b**)

Figure 22. PIL results of the load side waveforms: (**a**) load voltages; and (**b**) load current.

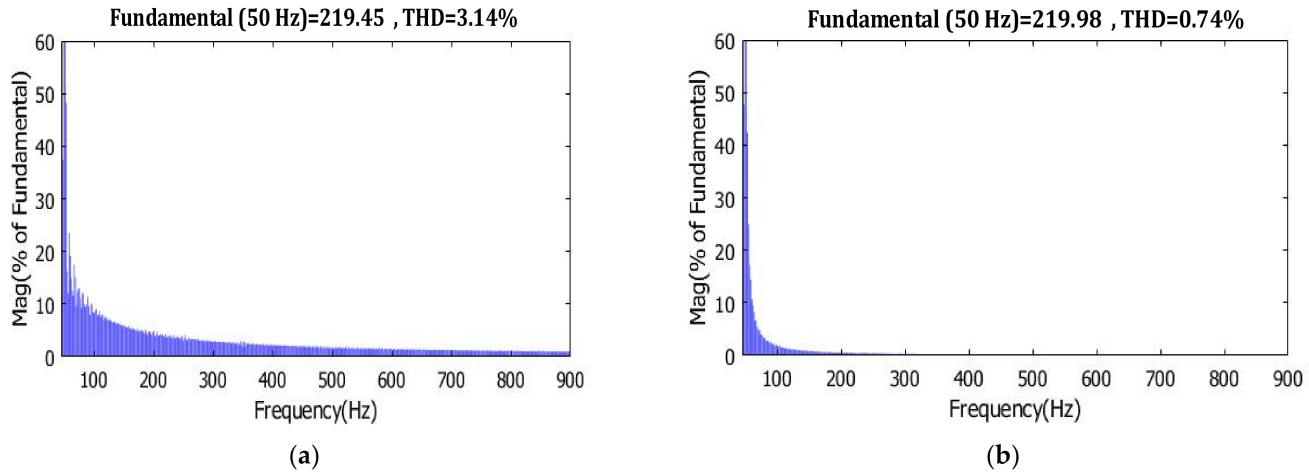

(**a**) (**b**)

Figure 23. Simulation results of the magnitude and THD load voltage: (**a**) the traditional PI technique; and (**b**) the suggested ST-SMC based on the DLO scheme.

As a consequence, the co-simulation PIL technique may be used in a practical environment to verify the hardware validation of several process controls.

5. Conclusions

In this paper, a control scheme based on a super-twisting sliding mode control algorithm and a Luenberger current observer has been proposed. This scheme was implemented for a three-phase inverter to ensure an appropriate and smooth transition from the grid-connected mode to the island mode. In the control scheme, a current controller based on Luenberger's current observer was adopted for synchronizing the grid-connected inverter to the utility grid. While in the SA mode, an external voltage control loop within a cascaded voltage/current control scheme was designed based on a super-twisting algorithm. In addition, the Luenberger observer was also adopted for estimating the inverter-side current. The proposed control scheme contributed, in addition, to providing a seamless transition between both modes of operation and reducing the system cost by eliminating the current sensors. A simulation model and PIL system of a three-phase inverter within an MG were built in the PSIM environment to assess the efficiency of the designed control scheme. The presented results revealed that the suggested transition control guaranteed a seamless transfer between the GC and SA modes without any undesirable distortions, as well as appropriate transient and steady-state performances during the GC and SA operating modes. The results indicate that the designed control provided a low-THD sinusoidal load voltage, which was reduced from 3.14% to 0.74%. Additionally, the estimated error was completely minimal, at around 0.1 V, validating the excellent estimation accuracy of the proposed Luenberger observer. In the near future, the proposed work can be expanded to experimentally validate the control approach for paralleled inverters functioning in GC and SA modes.

Author Contributions: Conceptualization, A.A. and K.D.; methodology, A.C., T.D. and P.B.; software, A.C. and A.H.; validation, A.C. and A.H.; formal analysis, A.A., K.D. and L.C.-A.; investigation, A.A., L.C.-A. and A.C.; resources, L.C.-A. and P.B.; data curation, K.D. and A.H.; writing—original draft preparation, A.A.; writing—review and editing, A.A., T.D. and P.B.; visualization, K.D. and T.D.; supervision, K.D. and L.C.-A.; project administration, T.D.; funding acquisition, L.C.-A. and P.B. All authors have read and agreed to the published version of the manuscript.

Funding: This research received no external funding.

Data Availability Statement: Not applicable.

Conflicts of Interest: The authors declare no conflict of interest.

References

1. Chaturvedi, S.; Wang, M.; Fan, Y.; Fulwani, D.; Hollweg, G.V.; Khan, S.A.; Su, W. Control Methodologies to Mitigate and Regulate Second-Order Ripples in DC–AC Conversions and Microgrids: A Brief Review. *Energies* **2023**, *16*, 817. [CrossRef]
2. Amer, A.; Shaban, K.; Gaouda, A.; Massoud, A. Home energy management system embedded with a multi-objective demand response optimization model to benefit customers and operators. *Energies* **2021**, *14*, 257. [CrossRef]
3. Anglani, N.; Di Salvo, S.R.; Oriti, G.; Julian, A.L. Steps towards Decarbonization of an Offshore Microgrid: Including Renewable, Enhancing Storage and Eliminating Need of Dump Load. *Energies* **2023**, *16*, 1411. [CrossRef]
4. Khan, M.A.; Kurukuru, V.B.; Haque, A.; Mekhilef, S. Islanding classification mechanism for grid-connected photovoltaic systems. *IEEE J. Emerg. Sel. Top. Power Electron.* **2020**, *9*, 1966–1975. [CrossRef]
5. Ochs, D.S.; Mirafzal, B.; Sotoodeh, P. A method of seamless transitions between grid-tied and stand-alone modes of operation for utility-interactive three-phase inverters. *IEEE Trans. Ind. Appl.* **2013**, *50*, 1934–1941. [CrossRef]
6. Mahmoud, A.A.; Hafez, A.A.; Yousef, A.M.; Gaafar, M.A.; Orabi, M.; Ali, A.F. Fault-tolerant modular multilevel converter for a seamless transition between stand-alone and grid-connected microgrid. *IET Power Electron.* **2023**, *16*, 11–25. [CrossRef]
7. Karimi-Ghartemani, M.; Khajehoddin, S.A.; Piya, P.; Ebrahimi, M. Universal controller for three-phase inverters in a microgrid. *IEEE J. Emerg. Sel. Top. Power Electron.* **2016**, *4*, 1342–1353. [CrossRef]
8. Yi, Z.; Dong, W.; Etemadi, A.H. A unified control and power management scheme for PV-battery-based hybrid microgrids for both grid-connected and islanded modes. *IEEE Trans. Smart Grid* **2017**, *9*, 5975–5985. [CrossRef]
9. Shi, K.; Zhou, G.; Xu, P.; Ye, H.; Tan, F. The integrated switching control strategy for grid-connected and islanding operation of micro-grid inverters based on a virtual synchronous generator. *Energies* **2018**, *11*, 1544. [CrossRef]
10. Lim, K.; Choi, J. Seamless grid synchronization of a proportional+ resonant control-based voltage controller considering non-linear loads under islanded mode. *Energies* **2017**, *10*, 1514. [CrossRef]

11. Lim, J.U.; Kwon, I.S.; Kim, H.W.; Cho, K.Y. Seamless Transfer Algorithm of AC Microgrid Inverter Compensating Load Current for Weak Grid. *Energies* **2019**, *12*, 728. [CrossRef]
12. Teng, Q.; Xu, D.; Yang, W.; Li, J.; Shi, P. Neural network-based integral sliding mode backstepping control for virtual synchronous generators. *Energy Rep.* **2021**, *7*, 1–9. [CrossRef]
13. Arafat, M.N.; Palle, S.; Sozer, Y.; Husain, I. Transition control strategy between standalone and grid-connected operations of voltage-source inverters. *IEEE Trans. Ind. Appl.* **2012**, *48*, 1516–1525. [CrossRef]
14. Vilhena, N.; Roncero-Clemente, C.; Delgado-Gomes, V.; Fernão Pires, V.; Martins, J.F. Energy router for SC: GC, SA and transition mode controls. *IET Renew. Power Gener.* **2020**, *14*, 914–924. [CrossRef]
15. Lim, K.; Choi, J. PR based indirect current control for seamless transfer of grid-connected inverter. In Proceedings of the 2016 IEEE 8th International Power Electronics and Motion Control Conference (IPEMC-ECCE Asia), Hefei, China, 22–26 May 2016; pp. 3749–3755.
16. Benadli, R.; Bjaoui, M.; Khiari, B.; Sellami, A. Sliding Mode Control of Hybrid Renewable Energy System Operating in Grid Connected and Stand-Alone Mode. *Power Electron. Drives* **2021**, *6*, 144–166. [CrossRef]
17. Mohamed, Y.A.R.I.; Radwan, A.A. Hierarchical control system for robust microgrid operation and seamless mode transfer in active distribution systems. *IEEE Trans. Smart Grid* **2011**, *2*, 352–362. [CrossRef]
18. Canciello, G.; Russo, A.; Guida, B.; Cavallo, A. Supervisory control for energy storage system onboard aircraft. In Proceedings of the 2018 IEEE International Conference on Environment and Electrical Engineering and 2018 IEEE Industrial and Commercial Power Systems Europe (EEEIC/I&CPS Europe), Palermo, Italy, 12–15 June 2018; pp. 1–6.
19. Li, X.; Zhang, H.; Shadmand, M.B.; Balog, R.S. Model predictive control of a voltage-source inverter with seamless transition between islanded and grid-connected operations. *IEEE Trans. Ind. Electron.* **2017**, *64*, 7906–7918. [CrossRef]
20. Choe, J.M.; Byen, B.J.; Moon, S.; Lai, J.S. A capacitor current control for stand-alone inverters using an inductor current observer. In Proceedings of the 2015 IEEE 9th International Conference on Power Electronics and ECCE Asia (ICPE-ECCE Asia), Seoul, Republic of Korea, 1–5 June 2015; pp. 1143–1148.
21. Latham, J.; Mohebbi, M.; McIntyre, M.L. Output feedback control of a single phase voltage source inverter utilizing a variable structure observer. In Proceedings of the 2017 IEEE American Control Conference (ACC), Seattle, WA, USA, 24–26 May 2017; pp. 4081–4086.
22. Lou, G.; Gu, W.; Wang, J.; Wang, J.; Gu, B. A unified control scheme based on a disturbance observer for seamless transition operation of inverter-interfaced distributed generation. *IEEE Trans. Smart Grid* **2017**, *9*, 5444–5454. [CrossRef]
23. Zhang, Z.; Wu, J.; Zheng, L.; Xie, D.; Tang, X. An Inductor Current Sensorless Control Strategy Based on Modified VSG Method for Single-Phase Microgrid Application with Seamless Transfer Capability. *Front. Energy Res.* **2021**, *9*, 575. [CrossRef]
24. Cheng, C.; Xie, S.; Xu, J.; Qian, Q. State-and-disturbance-observer-based current control scheme for LCL-filtered single-phase grid-tied inverters under nonideal conditions. *IEEE J. Emerg. Sel. Top. Power Electron.* **2021**, *10*, 336–348. [CrossRef]
25. Vegunta, S.C.; Higginson, M.J.; Kenarangui, Y.E.; Li, G.T.; Zabel, D.W.; Tasdighi, M.; Shadman, A. AC microgrid protection system design challenges—A practical experience. *Energies* **2021**, *14*, 2016. [CrossRef]
26. Hren, A.; Mihalič, F. An improved SPWM-based control with over-modulation strategy of the third harmonic elimination for a single-phase inverter. *Energies* **2018**, *11*, 881. [CrossRef]
27. Guo, B.; Su, M.; Wang, H.; Tang, Z.; Liao, Y.; Zhang, L.; Shi, S. Observer-based second-order sliding mode control for grid-connected VSI with LCL-type filter under weak grid. *Electr. Power Syst. Res.* **2020**, *183*, 106270. [CrossRef]
28. Aillane, A.; Dahech, K.; Damak, T.; Chouder, A.; Hadjkaddour, A.; Cherifi, A. An Observer-Based Inductor Current Control for a Bifunctional Three-Phase DG-Inverter. In Proceedings of the 2022 IEEE 21st international Conference on Sciences and Techniques of Automatic Control and Computer Engineering (STA), Sousse, Tunisia, 19–21 December 2022; pp. 566–571.
29. Khan, M.A.; Haque, A.; Kurukuru, V.S.B. Droop based Low voltage ride through implementation for grid integrated photovoltaic system. In Proceedings of the 2019 IEEE International Conference on Power Electronics, Control and Automation (ICPECA), New Delhi, India, 16–17 November 2019; pp. 1–5.
30. Hmad, J.; Houari, A.; Trabelsi, H.; Machmoum, M. Fuzzy logic approach for smooth transition between grid-connected and stand-alone modes of three-phase DG-inverter. *Electr. Power Syst. Res.* **2019**, *175*, 105892. [CrossRef]
31. Russo, A.; Canciello, G.; Cavallo, A. Generalized super-twisting control of a dual active bridge for more electric aircraft. In Proceedings of the 2021 European Control Conference (ECC), Delft, The Netherlands, 29 June–2 July 2021; pp. 1610–1615.
32. Ammar, A.; Benakcha, A.; Bourek, A. Closed loop torque SVM-DTC based on robust super twisting speed controller for induction motor drive with efficiency optimization. *Int. J. Hydrogen Energy* **2017**, *42*, 17940–17952. [CrossRef]
33. Rashed, M.; Goh, K.B.; Dunnigan, M.W.; MacConnell, P.F.A.; Stronach, A.F.; Williams, B.W. Sensorless second-order sliding-mode speed control of a voltage-fed induction-motor drive using nonlinear state feedback. *IEE Proc. Electr. Power Appl.* **2005**, *152*, 1127–1136. [CrossRef]
34. Levant, A. Higher-order sliding modes, differentiation and output-feedback control. *Int. J. Control* **2003**, *76*, 924–941. [CrossRef]
35. Bendjeddou, Y.; Deboucha, A.; Bentouhami, L.; Merabet, E.; Abdessemed, R. Super twisting sliding mode approach applied to voltage orientated control of a stand-alone induction generator. *Prot. Control Mod. Power Syst.* **2021**, *6*, 18. [CrossRef]
36. Deffaf, B.; Hamoudi, F.; Debdouche, N.; Amor, Y.A.; Medjmadj, S. Super-twisting Sliding Mode Control for a Multifunctional Double Stage Grid-connected Photovoltaic System. *Adv. Electr. Electron. Eng.* **2022**, *20*, 240–249. [CrossRef]

37. Vardhan, H.; Akin, B.; Jin, H. A low-cost, high-fidelity processor-in-the loop platform: For rapid prototyping of power electronics circuits and motor drives. *IEEE Power Electron. Mag.* **2016**, *3*, 18–28. [CrossRef]
38. Çelik, D. Lyapunov based harmonic compensation and charging with three phase shunt active power filter in electrical vehicle applications. *Int. J. Electr. Power Energy Syst.* **2022**, *136*, 107564. [CrossRef]